Nanoscale

Accepted Manuscript

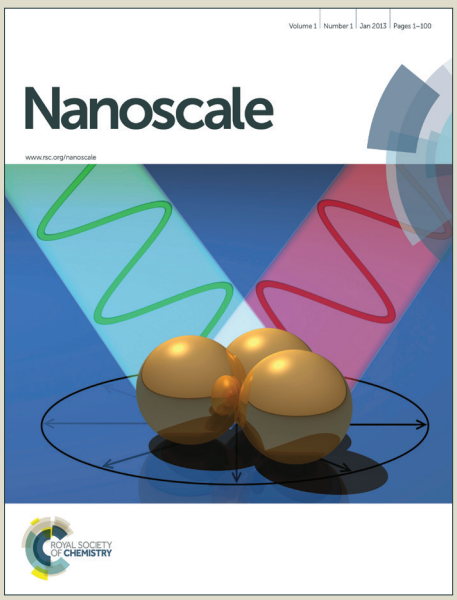

ROYAL SOCIETY OF CHEMISTRY

www.rsc.org/nanoscale

Cite this: DOI: 10.1039/c0xx00000x

www.rsc.org/xxxxxx

Communication

Facile synthesis of hierarchical dendritic PtPd nanogarlands supported on reduced graphene oxide with enhanced electrocatalytic properties

Shan-Shan Li,[a] Jie-Ning Zheng,[a] Xiaohong Ma,[b] Yuan-Yuan Hu,[a] Ai-Jun Wang,[a]*Jian-Rong Chen [a] and Jiu-Ju Feng [a]*

Received (in XXX, XXX) Xth XXXXXXXXX 200X, Accepted Xth XXXXXXXXX 200X
DOI: 10.1039/b000000x

A simple and facile method is developed for one-pot preparation of hierarchical dendritic PtPd nanogarlands supported on reduced graphene oxide (PtPd/RGO) at room temperature, without using any seed, organic solvent, or complex apparatus. It is found that octylphenoxypolye thoxyethanol (NP-40) as a soft template and its amount are critical to the formation of the PtPd garlands. The as-prepared nanocomposites are further applied to methanol and ethanol oxidation with significantly enhanced electrocatalytic activity and better stability in alkaline media.

1 Introduction

Direct alcohol fuel cells (DAFCs) based on liquid fuels have attracted enormous attention as power sources for portable electronic devices and fuel-cell vehicles, owing to their much higher energy density.[1, 2] Furthermore, their storage and transport are much easier than hydrogen,[3] and thereby great progress has been made in fuel-cell science and technology, especially in the synthesis of Pt-based nanocatalysts.[4-6] However, their commercialization is severely hampered by high cost, sluggish kinetics, and poor stability.[1, 7, 8] Therefore, it is highly desirable to prepare novel catalysts with improved performance.

Recent advances reveal that accurate controlling the size, shape, composition, and structures (solid, hollow, or porous) of a metallic catalyst would enhance its functions and performance.[9-14] Incorporation with a second metal component can bring the variations of particle size, shape, surface structures, catalytic activity, and chemical selectivity, as well as alloy structures. Compared with monometal systems, rational design of bimetallic nanostructures can provide enlarged surface area with more active sites available for the improvement of the catalytic property. Thus, a variety of bimetallic nanostructures have been prepared, such as tubes,[15] wires,[16] dendrites,[17] and flowers.[18] A good example is reduced graphene oxide (RGO) supporting porous PtPd nanospheres with the enhanced catalytic activity toward methanol oxidation reaction.[19]

Impressively, PtPd bimetallic nanostructures have received increasing attention because of their efficient catalytic performance,[17, 20-22] and hence many methods have been developed, including wet-chemical synthesis,[4, 19, 20] electrodeposition,[23, 24] thermal treatment,[15, 25] and self-assembly.[3, 26] For example, Wang and coworkers synthesized Pt-on-Pd bimetallic nanodendrites supported on graphene nanosheets by a three-step wet-chemical method.[27] Xia's group fabricated Pt–Pd nanodendrites using Pd nanoparticles as seeds.[20] Chen and coworkers reported a facile and green method to fabricate PtPd alloy nanoparticles on graphene nanosheets in ethanol.[28] Chen's group prepared graphene-supported PtPd alloy nanocubes via a one-pot hydrothermal synthetic strategy.[8] Nevertheless, the above methods suffer from relatively high cost, complicated reaction steps, organic solvent, and rigorous operation skills. Impressively, aqueous wet-chemical synthesis is thought to be the favorable and environmentally friendly route to precisely control the Pt–Pd alloy nanostructures.[29] Therefore, it is always desirable to explore more economic, facile, and green solution-phase methods for preparation of Pt–Pd nanostructures with superior properties.

It is known that severe corrosion and oxidation of carbon supports in harsh operating environment would cause quick loss of the catalytic activity of a catalyst.[30] Thus, the supports play an important role, as demonstrated by previous studies, in which an ideal support would have a large surface area, good electrical conductivity, and high chemical stability. Lately, graphene has attracted significant attention, owing to its high theoretical surface area, excellent electrical conductivity, good thermal/chemical stability, extraordinary mechanical strength and flexibility, and strong adhesion to a catalyst,[31-33] along with widespread applications.[34-36] Therefore, graphene can fix and disperse a catalyst to ensure its stable deposition on the support, which is very helpful to maintain its original shape, size, and surface state during the catalytic reaction.[37] Furthermore, the graphene supporting catalyst displays poorer colloidal stability than the isolated one, because of the decrease in Brownian motions, which allows the catalyst to be easily collected and recycled from the reaction system as a bulk material.[37]

Herein, a facile and general synthetic method was developed for one-pot preparation of hierarchical dendritic garland-like PtPd nanostructures supported on reduced graphene oxide (PtPd/RGO) at room temperature, without any seed, organic solvent, or complex apparatus. The as-prepared nanocomposites were further applied to methanol and ethanol oxidation in alkaline media.

2 Results and discussion

Fig. 1A shows the representative transmission electron microscopy (TEM) images of the porous garland-like PtPd nanostructures deposited on the RGO, with an average diameter of 100.32 ± 0.50 nm, based on the particle size distribution. The porous structure can be confirmed by low-angle X-ray diffraction (XRD) spectrum for the PtPd/RGO with a characteristic diffraction peak at around 1.68° (Fig. S1).[38] These observations (Fig. 1A and 1B) are quite different from individual Pt (Fig. S2A)

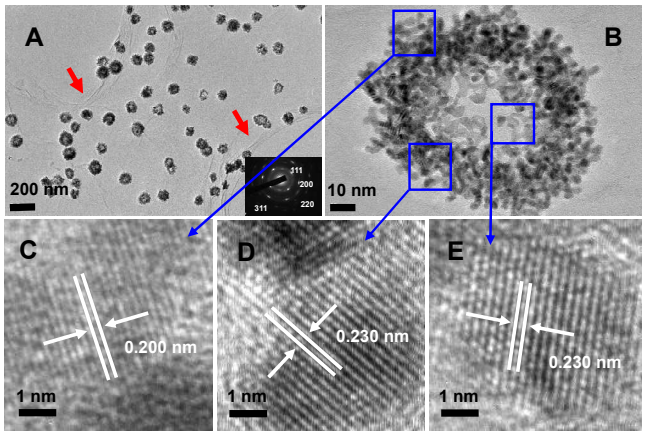

Fig. 1 TEM (A) and HRTEM (B, C, D, E) images of the garland-like PtPd/RGO. Insets show the SAED patterns marked in different positions. Red arrows indicate the wrinkles of the RGO.

and Pd (Fig. S2B) supported on the RGO, owing to the critical role of octylphenoxypolye thoxyethanol (NP-40) as a soft template.[19, 25, 39] As expected, the absence of NP-40 yields irregular solid particles, while other conditions are kept the same (Fig. S3A). Moreover, insufficient NP-40 induces the formation of similar porous PtPd structures with the decreased quality, and flower-like PtPd nanostructures are emerged using excessive NP-40 (Fig. S3B-D), rather than the garland-like PtPd nanostructures.

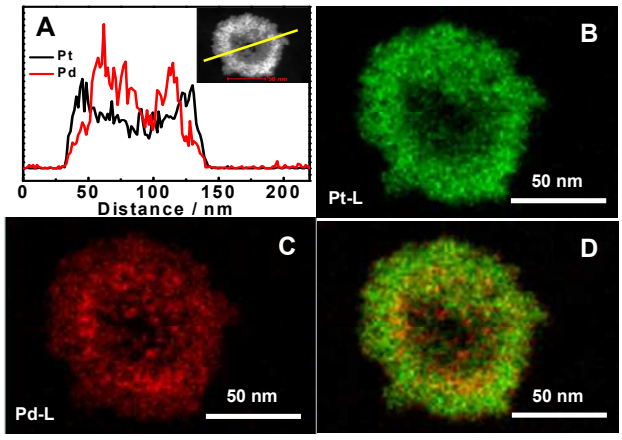

Fig. 2 Cross-sectional compositional line profiles (A) taken from a garland-like PtPd nanoparticle. HAADF-STEM-EDS elemental mapping images of Pt-L (B), Pd-L (C), and Pt-Pd (D). Inset shows the HAADF-STEM image of a single garland-like PtPd nanoparticle.

These results indicate that NP-40 and its amount are critical to the formation of the hierarchical PtPd garlands. Impressively, the wrinkles of the RGO nanosheets can be clearly observed in Fig.1A and Fig. S4, confirming the existence of RGO.

Besides, a mixed diffraction pattern is observed from the selective area electron diffraction (SAED) measurements (inset in Fig. 1A), corresponding to the (111), (200), (220), and (311) planes from inside to outside. Moreover, high resolution TEM (HRTEM) images reveal well crystallization of the PtPd alloy with lattice spacing distances of 0.200 nm (Fig. 1C) and 0.230 nm (Fig. 1D and 1E), which are assigned to the (200) and (111) planes of the face-centered cubic (fcc) PtPd, respectively.[10, 25, 40] The distribution of each element in the PtPd alloy was examined by high-angle annular dark-field scanning transmission electron microscope energy dispersive X-ray spectroscopy (HAADF-STEM-EDS) measurements (Fig. 2). The cross-sectional compositional line profiles (Fig. 2A) and the image of a single garland-like PtPd nanoparticle obtained by HAADF-STEM (inset in Fig. 2A) both evidence the PtPd alloy with hollow structures and homogenous distribution, as further confirmed by the EDS elemental mapping images (Fig. 2B-D).

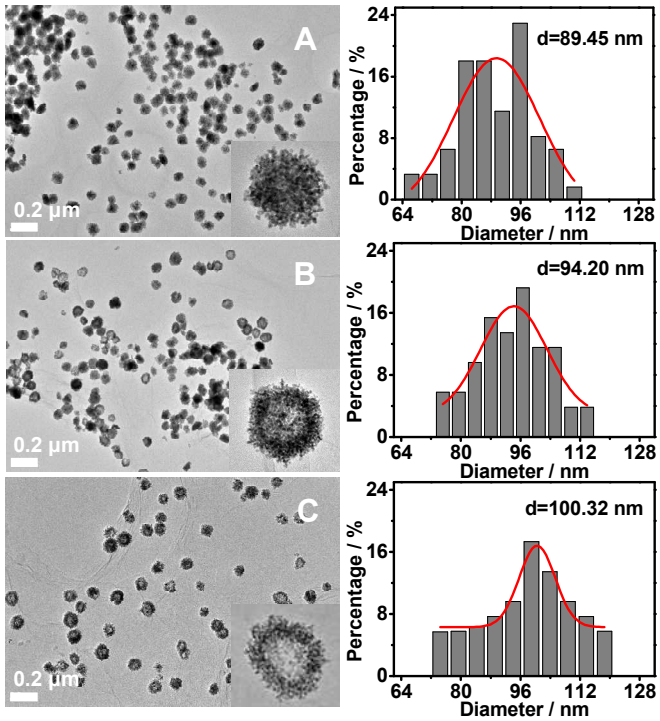

Fig. 3 TEM images of the PtPd/RGO obtained with the reaction time of 0.5 h (A), 8 h (B), and 12 h (C), along with the corresponding particle size distribution, respectively.

The NP-40 molecules adsorb onto the PtPd alloy surface and form a surfactant layer via a thermodynamically driven process at the surface/interface.[41] The resulting surfactant layer is generally not uniform because the adsorbated molecules are thermodynamically unstable. Thus, many unstable sites are formed because of the intrinsic dynamic nature of the surfactant itself. At the same time, more unstable sites are also found on the

intergrain boundaries associated with the characteristics of the PtPd alloy, inducing the reconstruction of the PtPd nanostructure, and vice versa affect the quality of the surfactant layer.

A possible formation mechanism of inside-out Ostwald ripening is developed to illustrate the formation of the garland-like nanostructures.[42, 43] At the very initial stage, the dendritic nanospheres are formed by reducing the precursors with the assistance of NP-40 (Fig. 1-2 and Fig. S3B-D). The nanoparticles in the center are initially and rapidly formed, which might have high surface energy or surface tension, and low degree of crystallinity, compared with the outside nanoparticles.[44, 45] Furthermore, the inner nanoparticles might have slight bending in the dendritic nanospheres, and thereby the surface of the nanoparticles are unevenly covered by the NP-40 molecules, inducing the formation of the unstable crystal sites.[41, 44, 45] As a result, its inner part has a strong tendency to dissolve and reconstruct, which provides the driving force for spontaneously inside-out Ostwald ripening (Fig. 3 and Fig. S4). This assumption is strongly demonstrated by our time-control experiments (Fig. 3), where the average diameter of the dendritic nanospheres changes from 89.45 to 100.32 nm during the Ostwald ripening. With the reaction time of 36 h, the inner core is further dissolved and the rings become large and thin because of the reconstruction, accompanied with the appearance of some broken ones (Fig. S4, Supporting Information).

The EDS pattern (Fig. S5A) reveals that Pt and Pd are predominant species, and the molar ratio of Pt to Pd is ca. 2:1 in the PtPd/RGO. Besides, C, O, and Cu elements are also detected. The peak of C comes from the RGO and supporting film of the copper grid, while the oxygen signal is originated from incomplete reduction of the GO.[46] Additionally, the signals from Cu are indexed to the copper grid used for the TEM experiments.

Fig. S5B shows the wide-angle X-ray diffraction (XRD) patterns of the PtPd/RGO (curve a), Pt/RGO (curve b), Pd/RGO (curve c), RGO (curve d), and GO (curve e), respectively. For the PtPd/RGO (curve a), there are four representative diffraction peaks at 40.0°, 46.5°, 68.1°, and 82.0°, corresponding to the (111), (200), (220), and (311) planes of the PtPd alloy.[8, 15, 47] These peaks are located between individual Pt (curve b) and Pd (curve c) supported on the RGO, confirming the alloy formation between Pt and Pd,[48, 49] as demonstrated by the SAED measurements (inset in Fig. 1A). Additionally, a broad diffraction peak at around 23.0° is attributed to the disorderedly stacked RGO (curve d), different from the GO (curve e) only with a strong peak at 11.0° corresponding to the (002) planes of the GO.

In order to study the chemical states during chemical reduction, X-ray photoelectron spectra (XPS) were employed to analyze the PtPd/RGO. As illustrated in Fig. S6A, the dominant XPS peaks at 74, 286, 336, and 534 eV are assigned to Pt_{4f}, C_{1s}, Pd_{3d}, and O_{1s} in the survey spectrum, respectively. Table S1 provides their elemental components. Notably, the molar ratio of Pt to Pd is estimated to be 2:1, which is in good accordance with the EDS data (Fig. S5A). To identify the valence states of Pt, the Pt_{4f} spectrum (Fig. S6B) can be further deconvoluted into two components. The stronger peaks at 71.23 eV (Pt $4f_{7/2}$) and 74.48 eV (Pt $4f_{5/2}$) are ascribed to Pt^0, while the weaker ones at 72.89 eV (Pt $4f_{7/2}$) and 76.82 eV (Pt $4f_{5/2}$) correspond to Pt^{2+} in PtO or $Pt(OH)_2$.[50] Similar method is used to analyze the Pd valence states (Fig. S6C). The four peaks at 335.6 eV (Pd $3d_{5/2}$), 340.8 eV (Pd $3d_{3/2}$), 337.9 eV (Pd $3d_{5/2}$), and 343.3 eV (Pd $3d_{3/2}$) correspond to Pd^0 and Pd^{2+} species, respectively.[49, 51] By measuring their relative intensities, it is found that Pt^0 and Pd^0 are the predominant species, with the percentage of 92.0% and 66.7%, respectively, which have a close relation with the electrochemical activity.[52] Similarly, the peak from C_{1s} is further fitted into three peaks at 284.8 eV, 286.6 eV, and 287.9 eV (Fig. S6D), corresponding to the C–C (sp^2), C–O, and C=O groups, respectively.[8, 52] These observations confirm the effective reduction of the GO by the loss of oxygen moieties and formation of the C–C bonds, along with the significant decrease of the C–O groups.[8, 52]

Similarly, the effective reduction of the GO is further confirmed by Fourier transform infrared (FT-IR) spectra (Fig. S7A), in which the absorption peaks at 1060, 1228, 1407, 1734, and 1627 cm^{-1} correspond to the stretching vibrations of C–O, C–OH, O–H, C=O, and the skeletal vibration of C=C for the GO (curve a), respectively.[53, 54] Besides, the strong broad peak at 3430 cm^{-1} is attributed to the O–H stretching vibration of C–OH groups and water.[19] However, there are only a strong and two weak peaks corresponding to the O–H, C–O and C=C groups for the RGO (curve b), Pd/RGO (curve c), Pt/RGO (curve d), and PtPd/RGO (curve e), indicating the efficient removal of the oxygen-containing functional groups from the GO sample.

UV-vis absorption measurements were used to track the formation of the PtPd/RGO (Fig. S7B). For the GO sample (curve a), there is a peak detected at 228 nm and a shoulder emerged at 300 nm, corresponding to the π–π* transitions of the aromatic C=C bonds and the n–π* transitions of the C=O bands, respectively.[8, 53] However, the peak at 228 nm red shifts to 263 nm when the GO is reduced to RGO (curve b). Nevertheless, after the deposition of Pd, Pt, and PtPd nanoparticles on the RGO, the peak at 263 nm for the RGO blue shifts to 232 nm for the Pd/RGO (curve c), 237 nm for the Pt/RGO (curve d), and 240 nm for the PtPd/RGO (curve e), respectively, which are clearly located between the GO and RGO samples, along with higher baseline, suggesting the formation of the PtPd alloy.

Raman spectroscopy is widely employed to detect the crystalline structures of graphene-based materials. Fig. S8A shows the Raman spectra of the PtPd/RGO (curve a), Pt/RGO (curve b), Pd/RGO (curve c), RGO (curve d), and GO (curve e), respectively. For the PtPd/RGO (curve a), there are two peaks at 1326 and 1598 cm^{-1} ascribed to the *D* and *G* bands, respectively, with a little blue shift in comparison with that of the GO (curve e), revealing strong interactions between graphene and bimetallic nanostructures. The *D* band is associated with the A_{1g} breathing mode of disordered graphite structure, while the *G* band is related to the doubly degenerate E_{2g} of graphite.[19, 53] Meanwhile, the intensity ratio of the *D* to *G* bands (I_D/I_G) indicates the degree of disorder and average size of the in-plane sp^2 domains.[19, 53] The corresponding I_D/I_G ratios are increased as follows: PtPd/RGO > RGO > Pd/RGO > Pt/RGO, using the GO as the standard, implying the decreased size of the sp^2 domains and partially

ordered crystal structures of the resulting RGO.

Thermo gravimetric analysis (TGA) measurements were performed to accurately estimate the metal loading. The TGA curves of the PtPd/RGO (Fig. S8B, curve a) is similar to those of the Pt/RGO (Fig. S8B, curve b) and Pd/RGO (Fig. S8B, curve c), but quite different from that of the GO (Fig. S8B, curve d) under the same conditions, revealing the decrease of the quantity of the oxygen-containing functional groups on the graphene.[19, 52] Furthermore, the curves are gradually reached a plateau, unlike the GO (Fig. S8B, curve d), indicating high metal loading on the RGO. The corresponding weight percentage is around 90% for the PtPd, 78% for the Pt, and 57% for the Pd, respectively.

Fig. S9 shows the typical cyclic voltammograms of the PtPd/RGO (curve a), Pt/RGO (curve b), and Pd/RGO (curve c) catalysts modified electrodes in 0.5 M H_2SO_4. All the curves exhibit three traditional distinctive potential regions associated with hydrogen adsorption/desorption processes in the potential range of –0.20 ~ 0.10 V, the double layer is located from 0.10 to 0.40 V, and the formation/reduction of the surface oxide is emerged above 0.4 V.[8, 55] One can see that the capacitance of the double layer is much larger for the PtPd/RGO (curve a), compared with the Pt/RGO (curve b) and Pd/RGO (curve c) catalysts, showing higher current density of the PtPd/RGO. In the positive scan, metals/alloys are oxidized between 0.5 and 0.6 V, while the oxidized metals/alloys are reduced between 0.4 and 0.6 V in the reverse scan. It is observed that the reduction peak potential (E_p) of the PtPd/RGO (curve a) is located between the Pt/RGO (curve b) and Pd/RGO (curve c), suggesting the formation of the PtPd alloy on the RGO,[3] as confirmed by the XRD results.

CO-stripping voltammetry measurements were performed by oxidizing preadsorbed CO in 0.5 M H_2SO_4 (Fig. S10). The electrochemically active surface area (EASA) is 83.1 $m^2\ g^{-1}$ for the PtPd/RGO, which is much larger than those of the Pt/RGO (16.3 $m^2\ g^{-1}$), Pd/RGO (12.5 $m^2\ g^{-1}$), and commercial 10% Pd/C (19.7 $m^2\ g^{-1}$) catalysts under the identical conditions. Furthermore, the onset potential (E_{on}) of the PtPd/RGO (Fig. S10A) negatively shifts in comparison with the Pt/RGO (Fig. S10B), Pd/RGO (Fig. S10C), and commercial 10% Pd/C (Fig. S10D) catalysts. Thus, the PtPd/RGO has larger EASA and negatively- shifted E_{on}, which would benefit to the enhancement of the catalytic ability.

The electrocatalytic activity of the PtPd/RGO (curve a), Pt/RGO (curve b), Pd/RGO (curve c), commercial 10% Pt/C (curve d), and 10% Pd/C (curve e) catalysts modified electrodes were firstly investigated in 1.0 M KOH toward methanol (Fig. 4A) and ethanol (Fig. 4C) oxidation. In each case, the oxidation peak observed in the forward scan corresponds to methanol or ethanol oxidation, and another oxidation peak detected in the reverse scan is attributed to the removal of carbonaceous intermediates that are not completely oxidized in the forward scan. Table S2 lists the associated E_{on} and forward peak current density (j_F). One can see that more negative E_{on} and higher j_F are found for the PtPd/RGO. Meanwhile, the corresponding mass activities (MAs) toward methanol and ethanol oxidation are offered for comparison (Fig. 4B and 4D). Notably, the MAs are 333 and 298 mA mg^{-1} for the PtPd/RGO, which are much higher than those of the Pt/RGO (30 and 16 mA mg^{-1}), Pd/RGO (29 and 30 mA mg^{-1}), commercial 10% Pt/C (120 and 75 mA mg^{-1}), and 10% Pd/C (95 and 54 mA mg^{-1}) catalysts. Additionally, the electrocatalytic activity of the common PtPd nanoparticles/RGO modified electrode was also offered for comparison (Fig. S3A and Fig. S11). All these results reveal the improved electrocatalytic activity of the PtPd/RGO.

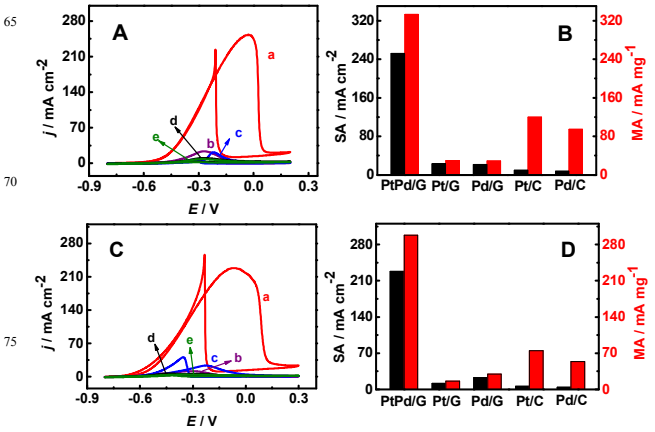

Fig. 4 Cyclic voltammograms of the PtPd/RGO (curve a), Pt/RGO (curve b), Pd/RGO (curve c), commercial 10% Pt/C (curve d), and 10% Pd/C (curve e) catalysts modified electrodes in 1.0 M KOH containing 1.0 M methanol (A) and 1.0 M ethanol (C). Comparison of the corresponding specific activity and mass activity.

The long term stability is one of the most important parameters for the applications of catalysts in fuel cells. To evaluate the electrochemical stability of the PtPd/RGO, chronoamperometry measurements were performed at the applied potential of –0.3 V in 1.0 M KOH containing 1.0 M methanol (Fig. 5A) and 1.0 M ethanol (Fig. 5C). Notably, an initial rapid current decay is observed, probably due to the formation of carbonaceous intermediates during methanol and ethanol oxidation reaction. After a long period of operation (2000 s), the PtPd/RGO shows a much lower deterioration rate and higher oxidation current in comparison with the other catalysts, although the current continues to decay, demonstrating better stability of the PtPd/RGO. Furthermore, the higher initial current is indicative of more active sites available for the PtPd/RGO. Additionally, the electrochemical stability of the PtPd/RGO is much better in comparison with the common PtPd nanoparticles/RGO (inset in Fig. S11).

To further examine the stability of the PtPd/RGO modified electrode, accelerated durability tests (ADTs) were performed in 1.0 M KOH containing 1.0 M methanol (Fig. 5B) and 1.0 M ethanol (Fig. 5D). The durability was tested by comparing the j_F and peak potentials (E_p) before and after an accelerated methanol and ethanol oxidation reaction. For example, using the j_F of the 20th cycle as a reference (inset in Fig. 5B), the j_F was only decreased to 96% after 100 cycles and 90% after 200 cycles. Using ethanol instead of methanol, the j_F still remains about 86% after 100 cycles and 72% after 200 cycles under the identical conditions (inset in Fig. 5D). Besides, the changes of the E_p are

between –0.04 and –0.05 V for methanol oxidation (Fig. S12A) and in the range of –0.21 to –0.24 V for ethanol oxidation (Fig. S12B), respectively. These results again indicate the enhanced durability of the PtPd/RGO in the present system. The improved electrocatalytic performance of the PtPd/RGO can be ascribed to larger EASA providing more active sites, the synergistic effects between Pt and Pd,[47] the high loading and good dispersion of the porous dendritic PtPd garlands on the RGO, and excellent electrical conductivity of the graphene.

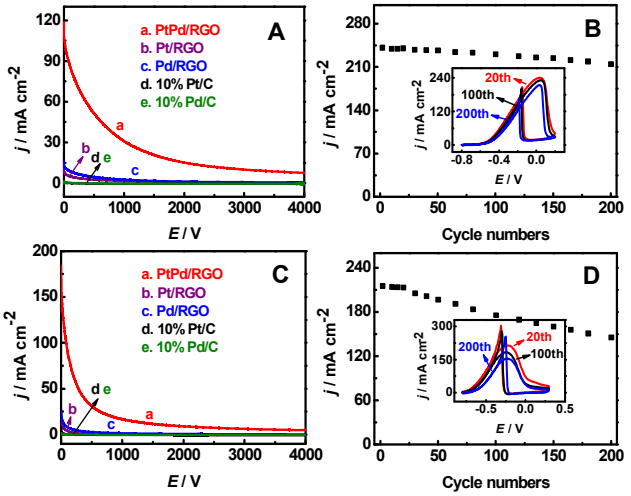

Fig. 5 Chronoamperometry curves of the PtPd/RGO (curve a), Pt/RGO (curve b), Pd/RGO (curve c), commercial 10% Pt/C (curve d), and 10% Pd/C (curve e) catalysts modified electrodes in 1.0 M KOH containing 1.0 M methanol (A) and 1.0 M ethanol (C). The forward peak current density as a function of potential scanning cycle of the PtPd/RGO modified electrode in 1.0 M KOH containing 1.0 M methanol (B) and 1.0 M ethanol (D). Insets show the corresponding 20th, 100th, and 200th cyclic voltammograms.

3 Conclusions

In summary, we have demonstrated a simple, facile and one-pot water-soluble approach for the fabrication of the porous dendritic PtPd nanogarlands on the RGO at room temperature, with the assistance of NP-40 as a soft template. The electrochemical experiments show that the as-prepared nanocomposites exhibit the significantly enhanced electrocatalytic activity and better stability toward methanol and ethanol oxidation in alkaline media, demonstrating its potential applications in fuel cells. The present work provides a facile method to synthesize graphene-supported alloy nanostructures, which would be very promising to prepare highly active and stable catalysts in practical applications.

Acknowledgements

This work was financially supported by the NSFC (Nos. 21175118, 21275130 and 21275131) and universities in Zhejiang province to the young academic leaders of academic climbing project (pd2013055).

Notes and references

[a] *College of Chemistry and Life Science, College of Geography and Environmental Science, Zhejiang Normal University, Jinhua, 321004, China*
[b] *State Key Laboratory of Multiphase Complex Systems, Institute of Process Engineering, Chinese Academy of Sciences, Beijing 100190, China*
**Corresponding author: jjfeng@zjnu.cn (JJF), ajwang@zjnu.cn (AJW).*

† Electronic Supplementary Information (ESI) available: (Experimental section, Fig. S1-S12 and Table S1-S2). See DOI: 10.1039/b000000x/

1 C. Lamy, A. Lima, V. Lerhun, F. Delime, C. Coutanceau and J.-M. Leger, *J. Power Sources,* 2002, **105**, 283-296.
2 M. K. Debe, *Nature,* 2012, **486**, 43-51.
3 C. Zhu, S. Guo and S. Dong, *Chem. Eur. J.,* 2013, **19**, 1104-1111.
4 B. Lim, J. Wang, P. H. C. Camargo, C. M. Cobley, M. J. Kim and Y. Xia, *Angew. Chem. Int. Ed.,* 2009, **48**, 6304-6308.
5 W. Xie, C. Herrmann, K. Kompe, M. Haase and S. Schlucker, *J. Am. Chem. Soc.,* 2011, **133**, 19302-19305.
6 L. Wang and Y. Yamauchi, *J. Am. Chem. Soc.,* 2010, **132**, 13636-13638.
7 A.-X. Yin, X.-Q. Min, Y.-W. Zhang and C.-H. Yan, *J. Am. Chem. Soc.,* 2011, **133**, 3816-3819.
8 Y. Lu, Y. Jiang, H. Wu and W. Chen, *J. Phys. Chem. C,* 2013, **117**, 2926-2938.
9 B. Y. Xia, H. B. Wu, X. Wang and X. W. Lou, *Angew. Chem. Int. Ed.,* 2013, **52**, 12337-12340.
10 L. Ruan, E. Zhu, Y. Chen, Z. Lin, X. Huang, X. Duan and Y. Huang, *Angew. Chem. Int. Ed.,* 2013, **52**, 12577-12581.
11 W. Zhang, J. Yang and X. Lu, *ACS Nano,* 2012, **6**, 7397-7405.
12 L.-F. Zhang, S.-L. Zhong and A.-W. Xu, *Angew. Chem. Int. Ed.,* 2013, **52**, 645-649.
13 L.-F. Zhang and C.-Y. Zhang, *Nanoscale,* 2013, **5**, 6074-6080.
14 L. Wang and Y. Yamauchi, *J. Am. Chem. Soc.,* 2013, **135**, 16762-16765.
15 Z. Chen, M. Waje, W. Li and Y. Yan, *Angew. Chem. Int. Ed.,* 2007, **46**, 4060-4063.
16 C. Koenigsmann, A. C. Santulli, K. Gong, M. B. Vukmirovic, W.-P. Zhou, E. Sutter, S. S. Wong and R. R. Adzic, *J. Am. Chem. Soc.,* 2011, **133**, 9783-9795.
17 L. Wang, Y. Nemoto and Y. Yamauchi, *J. Am. Chem. Soc.,* 2011, **133**, 9674-9677.
18 J. Xu, A. R. Wilson, A. R. Rathmell, J. Howe, M. Chi and B. J. Wiley, *ACS Nano,* 2011, **5**, 6119-6127.
19 S.-S. Li, J.-J. Lv, Y.-Y. Hu, J.-N. Zheng, J.-R. Chen, A.-J. Wang and J.-J. Feng, *J. Power Sources,* 2014, **247**, 213-218.
20 B. Lim, M. Jiang, P. H. C. Camargo, E. C. Cho, J. Tao, X. Lu, Y. Zhu and Y. Xia, *Science,* 2009, **324**, 1302-1305.
21 C. Venkateswara Rao, C. R. Cabrera and Y. Ishikawa, *J. Phys. Chem. C,* 2011, **115**, 21963-21970.
22 Y. Liu, M. Chi, V. Mazumder, K. L. More, S. Soled, J. D. Henao and S. Sun, *Chem. Mater.,* 2011, **23**, 4199-4203.
23 G. Ren and Y. Xing, *Nanotechnol. Mag.,* 2006, **17**, 5596-5601.
24 R. Ojani, J. B. Raoof and E. Hasheminejad, *Int. J. Hydrogen Energy,* 2013, **38**, 92-99.

25 X. Huang, Y. Li, Y. Li, H. Zhou, X. Duan and Y. Huang, *Nano Lett.,* 2012, **12**, 4265-4270.

26 S. Guo and S. Sun, *J. Am. Chem. Soc.,* 2012, **134**, 2492-2495.

27 S. Guo, S. Dong and E. Wang, *ACS Nano,* 2010, **4**, 547-555.

28 X. Chen, Z. Cai, X. Chen and M. Oyama, *J. Mater. Chem. A,* 2014, **2**, 315-320.

29 Y. Wang, S.-I. Choi, X. Zhao, S. Xie, H.-C. Peng, M. Chi, C. Z. Huang and Y. Xia, *Adv. Funct. Mater.,* 2014, **24**, 131-139.

30 Y.-J. Wang, D. P. Wilkinson and J. Zhang, *Chem. Rev.,* 2011, **111**, 7625-7651.

31 T. Maiyalagan, X. Dong, P. Chen and X. Wang, *J. Mater. Chem.,* 2012, **22**, 5286-5290.

32 S.-S. Li, J. Yu, Y.-Y. Hu, A.-J. Wang, J.-R. Chen and J.-J. Feng, *J. Power Sources,* 2014, **254**, 119-125.

33 X. Wang, X. Li, D. Liu, S. Song and H. Zhang, *Chem. Commun.,* 2012, **48**, 2885-2887.

34 X. Wan, Y. Huang and Y. Chen, *Acc. Chem. Res.,* 2012, **45**, 598-607.

35 C. Tan, X. Huang and H. Zhang, *Mater. Today,* 2013, **16**, 29-36.

36 X. Huang, X. Qi, F. Boey and H. Zhang, *Chem. Soc. Rev.,* 2012, **41**, 666-686.

37 X. Wang, D. Liu, S. Song and H. Zhang, *J. Am. Chem. Soc.,* 2013, **135**, 15864-15872.

38 H. Ataee-Esfahani, M. Imura and Y. Yamauchi, *Angew. Chem. Int. Ed.,* 2013, **52**, 13611-13615.

39 H. Wang, H. Y. Jeong, M. Imura, L. Wang, L. Radhakrishnan, N. Fujita, T. Castle, O. Terasaki and Y. Yamauchi, *J. Am. Chem. Soc.,* 2011, **133**, 14526-14529.

40 X. Huang, Y. Li, Y. Chen, E. Zhou, Y. Xu, H. Zhou, X. Duan and Y. Huang, *Angew. Chem. Int. Ed.,* 2013, **125**, 2580-2584.

41 J. C. Love, L. A. Estroff, J. K. Kriebel, R. G. Nuzzo and G. M. Whitesides, *Chem. Rev.,* 2005, **105**, 1103-1170.

42 C. C. Yec and H. C. Zeng, *J. Mater. Chem. A,* 2014, Accepted, DOI: 10.1039/c3ta14203e.

43 X. W. Lou, L. A. Archer and Z. Yang, *Adv. Mater.,* 2008, **20**, 3987-4019.

44 H. Yoo, J. Sharma, J. K. Kim, A. P. Shreve and J. S. Martinez, *Adv. Mater.,* 2011, **23**, 4431-4434.

45 J. Hu, K. Zhu, L. Chen, H. Yang, Z. Li, A. Suchopar and R. Richards, *Adv. Mater.,* 2008, **20**, 267-271.

46 L. Dong, R. R. S. Gari, Z. Li, M. M. Craig and S. Hou, *Carbon,* 2010, **48**, 781-787.

47 C. Zhu, S. Guo and S. Dong, *Adv. Mater.,* 2012, **24**, 2326-2331.

48 T. Lopes, E. Antolini and E. R. Gonzalez, *Int. J. Hydrogen Energy,* 2008, **33**, 5563-5570.

49 G. Fu, K. Wu, J. Lin, Y. Tang, Y. Chen, Y. Zhou and T. Lu, *J. Phys. Chem. C,* 2013, **117**, 9826-9834.

50 R. Chetty, S. Kundu, W. Xia, M. Bron, W. Schuhmann, V. Chirila, W. Brandl, T. Reinecke and M. Muhler, *Electrochim. Acta,* 2009, **54**, 4208-4215.

51 Y.-B. He, G.-R. Li, Z.-L. Wang, Y.-N. Ou and Y.-X. Tong, *J. Phys. Chem. C,* 2010, **114**, 19175-19181.

52 S. Sharma, A. Ganguly, P. Papakonstantinou, X. Miao, M. Li, J. L. Hutchison, M. Delichatsios and S. Ukleja, *J. Phys. Chem. C,* 2010, **114**, 19459-19466.

53 M. Liu, Y. Lu and W. Chen, *Adv. Funct. Mater.,* 2013, **23**, 1289-1296.

54 W. Yue, Z. Lin, S. Jiang and X. Yang, *J. Mater. Chem.,* 2012, **22**, 16318-16323.

55 W. He, H. Jiang, Y. Zhou, S. Yang, X. Xue, Z. Zou, X. Zhang, D. L. Akins and H. Yang, *Carbon,* 2012, **50**, 265-274.